Available online at https://link.springer.com/journal/42241
http://www.jhydrodynamics.com
Journal of Hydrodynamics, 2026, 38(4): 652-665
https://doi.org/10.1007/s42241-026-0070-5

Flow field analysis of ship turbulent wake flows and air-mixed wake flows

Jian-hua Wang[1], Xiao-song Zhang[2, 3], Qi-di Gao[1], Xin-yue Hu[1], Wen-tao Wang[4], De-cheng Wan[1*], Nick Markov[5]

1. *Computational Marine Hydrodynamics Lab (CMHL), School of Ocean and Civil Engineering, Shanghai Jiao Tong University, Shanghai 200240, China*
2. *China Ship Scientific Research Center Shanghai Branch, Shanghai 200011, China*
3. *CSSC Shanghai Marine Energy Saving Technology Co., Ltd., Shanghai 200011, China*
4. *China Ship Scientific Research Center, Wuxi 214082, China*
5. *Bulgarian Ship Hydrodynamics Center (BSHC), Bulgarian Academy of Sciences, Varna, Bulgarian*

(Received June 3, 2026, Revised July 28, 2026, Accepted August 11, 2026, Published online September 14, 2026)
©China Ship Scientific Research Center 2026

Abstract: Ship wake flows are critically important for hydrodynamic performance, particularly in ship resistance and propulsion. These turbulent wakes exhibit strong nonlinear behaviors, including vortex shedding and multi-scale vortex interactions. When air mixes into the wake, the vortical structures become even more complex. In order to better understand the physics of wake flows, it is quite important to find an appropriate approach to simulate and analyze the complex turbulent wake flows and air-mixed turbulent wake flows. In the present study, numerical methods including delayed detached eddy simulation (DDES), the Euler-Euler model, and vortical structure analysis methods were used to study the wake flow behaviors. The benchmark case of Japan Bulk Carrier (JBC) turbulence wake and the air-mixed wake flow of very large crude carrier (VLCC) model with air-layer drag reduction equipment were illustrated in detail. It is found that the energy spectra of the two main vortices of the JBC mainly characterize the energy-containing range and exhibit partial −5/3 scaling behavior over the inertial subrange. Deviations at higher wavenumbers, corresponding to smaller-scale motions, may arise from the combined effects of limited spatiotemporal resolution, numerical dissipation, and the possible deviation of Taylor's frozen turbulence hypothesis under highly unsteady wake conditions. For the air-mixed wake flows, some of the air is entrained downstream by the water flow in the form of discrete bubbles, enters the propeller flow field, and exerts a certain influence on the velocity distribution at the propeller disk plane.

Key words: Turbulence wake flow, delayed detached eddy simulation (DDES) method, Euler-Euler method, air-liquid mixed flow

0. Introduction

The wake of a ship hull is characterized by highly unsteady, strongly turbulent, and inherently complex flow structures, originating from hull-flow interactions, boundary-layer development, and stern separation processes. These mechanisms generate a broad range of complex turbulent motions. A detailed understanding of such complex turbulence features is essential for improving wake modelling and for supporting the development of high-fidelity computational fluid dynamics (CFD) approaches in ship hydrodynamics. Moreover, wake turbulence directly affects propulsion performance, energy-saving device effectiveness, and wake detectability, highlighting the need for systematic investigation of its complex characteristics. To address these challenges, the Wageningen 2025 Workshop on CFD in ship hydrodynamics (https://w2025.nl/) provides a dedicated benchmark for evaluating numerical methods against experimental data.

Currently, numerous methods are used for investigations of ship turbulence wakes. Experimental approaches have provided valuable insight into the 3-D development of ship turbulence wake. TUHH-FDS[1] measured the turbulent flow field around a JBC model under straight-ahead and drift-angle conditions using wind tunnel experiments, obtaining velocity components and Reynolds stresses, and analyzed stern flow separation, vortex structure evolution, and turbulent statistical characteristics. Stern et al.[2]

Project supported by the National Natural Science Foundation of China (Grant Nos. 52471335, 52131102).
Biography: Jian-hua Wang (1988-), Male, Ph. D., Associate Professor, E-mail: jianhuawang@sjtu.edu.cn
Corresponding author: De-cheng Wan, E-mail: dcwan@sjtu.edu.cn

employed 4-D particle tracking velocimetry to investigate the turbulence structure, vortex breakdown, and interactions of sonar dome vortices.

However, experimental methods are costly and data acquisition lacks sufficient flexibility. With the advancement of high-performance computing, CFD has become an essential tool for investigating ship wakes[3-4], offering greater flexibility in accessing 3-D flow structures and multiscale turbulence characteristics. Grlj et al.[5] employed Reynolds-averaged Navier-Stokes (RANS) equations with the shear stress transport (SST) k-ω turbulence model to systematically analyze the resistance and self-propulsion characteristics of the JBC ship at four different scales. However, this model cannot always provide satisfactory prediction results. The deficiency of the RANS model originates from the influence of pulsation. In the average flow fields, the eddy viscosity coefficient is isotropic, thus, the RANS model faces considerable challenges in predicting the anisotropic Reynolds stress. Additionally, researchers have explored other turbulence closure methods. Queutey et al.[6] used an anisotropic explicit algebraic Reynolds stress model to numerically simulate the flow field of the JBC with and without energy-saving ducts. The results showed that the predicted hull resistance was slightly lower than the experimental data, while the strength of the longitudinal bilge vortex in the wake prediction was slightly higher than the experimental data, with overall good agreement.

In addition to conventional RANS methods, hybrid RANS-LES methods have been applied to predict the wake field of the JBC ship. Studies have shown that the detached eddy simulations (DES) method can provide a more accurate stern wake, while traditional RANS methods yield coarser and smoother predictions of the stern wake. Such research demonstrates the advantages of advanced turbulence simulation techniques in capturing complex flow structures. Xing et al.[7] conducted DES of the Kyoto University Very Large Crude Carrier 2 (KVLCC2) at large drift angles, identifying complex vortex breakdown phenomena and multiple helical instability modes. Fureby et al.[8] compared RANS, large eddy simulation (LES), and hybrid RANS-LES approaches for the KVLCC2 hull under different drift angles, demonstrating the superiority of scale-resolving simulations in capturing instantaneous flow features. Feder et al.[9] employed the improved delayed detached eddy simulation (IDDES) numerical method to investigate the main wake vortices around a KVLCC2 hull at a static drift angle of $30°$. Spectral analysis indicated that the flow exhibits a low-frequency broadband wandering motion.

In addition to the above ship wake flow studies, a ship navigating in a marine environment will also encounter air-mixed flows. Such air-liquid mixed flows are widespread and exhibit diverse patterns. The bow wave breaking process also entrains air, thereby generating an air-mixed flow[10]. In addition to this passive generation mechanism, active air injection–such as in ship air lubrication technology–also produces air-mixed flows[11-12]. Regardless of the formation mechanism, the generation and evolution processes of these air-mixed flows involve intense multiphase flow dynamics and multi-physics mechanical characteristics, which significantly affect the hydrodynamic performance of ship structures[13].

Numerous studies have been conducted on ship air-mixed flows. Using experimental apparatus such as high-speed cameras and particle image velocimetry, underwater bubbles can be observed through physical experiments[14-16]. Alternatively, numerical simulations can be employed to investigate the flow characteristics and air distribution around the hull. Mainstream numerical methods include the volume of fluid method, the level-set method, and the Euler-Euler two-fluid method[17-20].

Beyond the flow characteristics of the air-liquid mixture around the ship itself, the air content in the propeller inflow has a direct impact on ship performance. The air content degrades propulsive efficiency, thereby affecting ship navigation and maneuverability[21]. Existing studies have shown that in open-water propeller experiments, forced air injection into the inflow directly reduces propeller thrust, and the magnitude of thrust reduction is closely related to the injection location[22]. Consequently, regardless of the generation mechanism, part of the air-mixed flow eventually reaches the stern, forming air-mixed wake flows. Currently, there are few studies on the air-mixed wake flow of ships. Most existing research focuses only on flat plates and centers on the effects of air-liquid mixed flow on boundary layer behavior. However, the air-mixed wake flow does have a significant impact on ship propulsion performance. Therefore, research on the air-mixed wake flows at the ship stern–including mean wake fraction, air content in the wake field, and air distribution near the stern–is of great significance.

The Japan Bulk Carrier (JBC) is a widely used benchmark hull form, and its wake characteristics have been widely investigated, providing valuable references for stern-flow and wake analyses. In the

present study, building on recent work with the 2025 JBC turbulence benchmark case, a scale-resolving simulation (SRS) approach based on the delayed detached eddy simulation (DDES) method with 5×10^9 grid cells was used to study the JBC wake flows. Compared with conventional RANS approaches, DDES provides an enhanced capability to capture large-scale unsteady turbulent structures while maintaining reasonable computational efficiency for high Reynolds number ship flows. Although IDDES further extends the hybrid RANS-LES framework, DDES is selected in the present study due to its demonstrated capability and computational efficiency for complex separated flows[23]. The resistance, wave pattern, velocity distribution, flow separation, and vortex analysis were analyzed. In addition, this paper also presents a numerical study of the ship air-mixed wake flow. Numerical simulations are carried out for a specially designed very large crude carrier (VLCC) equipped with an air layer drag reduction device. The characteristics of the air-mixed wake field at the stern, the flow behavior of the air-mixed wake, and the air distribution are investigated.

1. Numerical approaches

1.1 *delayed detached eddy simulation method*

In the simulation of the JBC ship wake field, accurate resolution of both the near-wall boundary layer and the large-scale unsteady vortical structures in the far wake is required. To achieve a balance between computational cost and fidelity, a SRS approach based on the DDES turbulence model is employed. The key idea of DDES is to formulate a hybrid length scale (L_{DDES}) that blends RANS and LES modes through a shielding function:

$$L_{\mathrm{DDES}} = L_{\mathrm{RANS}} - f_{\mathrm{d}} \max(0, L_{\mathrm{RANS}} - L_{\mathrm{LES}}) \tag{1}$$

In the near-wall region, where the boundary layer remains attached, the RANS length scale L_{RANS} is active; when the local grid spacing is sufficiently fine and flow separation occurs, the LES length scale L_{LES} takes over. These two length scales are defined respectively as:

$$L_{\mathrm{RANS}} = \frac{\sqrt{k}}{C_{\mu}\omega} \tag{2}$$

$$L_{\mathrm{LES}} = C_{\mathrm{DES}}\Delta \tag{3}$$

where k is the turbulent kinetic energy, ω is the specific dissipation rate, C_{μ} is a model constant, C_{DES} is a calibrated coefficient, and Δ is the local grid scale. The shielding function f_{d} is introduced to prevent premature switching to LES mode inside the boundary layer, which could otherwise trigger artificial flow separation. It is defined as:

$$f_{\mathrm{d}} = 1 - \tanh(512 r_{\mathrm{d}}^3) \tag{4}$$

$$r_{\mathrm{d}} = \frac{\nu_{\mathrm{t}} + \nu}{\sqrt{u_{ij}u_{ji}}\kappa^2 d^2} \tag{5}$$

where r_{d} is a dimensionless parameter, ν_{t} and ν are the turbulent and molecular kinematic viscosities, $\sqrt{u_{ij}u_{ji}}$ represents the magnitude of the velocity gradient tensor, κ is the von Kármán constant, and d is the distance to the nearest wall. The function f_{d} takes values close to 0 inside the boundary layer (where RANS dominates) and approaches 1 in separated flow regions (where LES is activated).

When the DDES framework operates in RANS mode, the flow is modeled using the SST k-ω turbulence model for closure. In contrast, when the local grid resolution and flow conditions trigger the LES mode, the hybrid DDES approach thus retains the efficiency of RANS in the attached boundary layer while recovering the resolving power of LES in separated and wake regions.

Finally, to account for the effect of the free surface, a two-phase flow model is adopted. The air-water interface is captured using the volume of fluid method, which solves an additional transport equation for the phase fraction.

The flow field is analyzed using the Q-criterion for vortex identification, and the Q-max method for vortex core extraction. The Q-criterion is defined as the second invariant of the velocity gradient tensor, which can be expressed as:

$$Q = \frac{1}{2}\left(\|\boldsymbol{\Omega}\|^2 - \|\boldsymbol{S}\|^2\right) \tag{6}$$

where $\boldsymbol{\Omega}$ and $\boldsymbol{S}$ are the vorticity and strain rate tensors, respectively. Positive Q values indicate rotation-dominated regions, corresponding to coherent vortex structures.

The definitions related to the turbulent energy spectra are given as follows:

$$E_{11}(\kappa_1) = \frac{\bar{U}}{\pi}\left\langle u^2 \right\rangle \hat{R}_E(2\pi\omega) \tag{7}$$

where $\bar{U}$ is the mean velocity, u represents the fluctuating velocity component, $\hat{R}_E(2\pi\omega)$ is obtained from the FFT of the temporal autocorrelation function $R_E(\tau)$ [24].

1.2 *Euler-Euler method*

In this research, the Euler-Euler two-fluid

method is employed as the numerical approach for simulating air-mixed wake flows. The interfacial area transport equation method is additionally incorporated to model bubble coalescence and breakup phenomena. Numerical simulations are performed using the open-source CFD platform OpenFOAM. The governing equations of the Euler-Euler method are expressed as:

$$\frac{\partial(\alpha_\varphi \rho_\varphi)}{\partial t} + \nabla \cdot (\alpha_\varphi \rho_\varphi \boldsymbol{U}_\varphi) = 0 \tag{8}$$

$$\begin{aligned} &\frac{\partial(\alpha_\varphi \rho_\varphi \boldsymbol{U}_\varphi)}{\partial t} + \nabla \cdot (\alpha_\varphi \rho_\varphi \boldsymbol{U}_\varphi \boldsymbol{U}_\varphi) \\ &= -\alpha_\varphi \nabla p + \nabla \cdot (\alpha_\varphi \boldsymbol{\tau}_\varphi) + \alpha_\varphi \rho_\varphi \boldsymbol{g} + \boldsymbol{F}_\mathrm{i} \end{aligned} \tag{9}$$

where the subscript φ denotes a certain phase, representing the quantities of water and air respectively, α represents the phase fraction, ρ represents the density of a certain phase, $\boldsymbol{U}$ represents the velocity, represents the viscous stress, $\boldsymbol{g}$ represents gravity, $\boldsymbol{F}_\mathrm{i}$ represents the interphase force, the $\boldsymbol{\tau}_\varphi$ is viscous stress term, and $\boldsymbol{F}_\mathrm{i}$ accounts for the force exerted by one phase on another phase, expressed by the following equation:

$$\boldsymbol{F}_\mathrm{i} = \boldsymbol{F}_\mathrm{d} + \boldsymbol{F}_\mathrm{l} + \boldsymbol{F}_\mathrm{t} + \boldsymbol{F}_\mathrm{w} + \boldsymbol{F}_\mathrm{v} \tag{10}$$

where $\boldsymbol{F}_\mathrm{d}$ represents the drag force, $\boldsymbol{F}_\mathrm{l}$ is the lift force, $\boldsymbol{F}_\mathrm{t}$ is the turbulent dispersion force, $\boldsymbol{F}_\mathrm{w}$ is the wall lubrication force, and $\boldsymbol{F}_\mathrm{v}$ is the virtual mass force. The lift force and wall lubrication force are not taken into account in this study.

To describe the motion and distribution of bubbles in the flow, the interfacial area transport equation (IATE) is used, which is expressed as:

$$\begin{aligned} &\frac{\partial a_\mathrm{i}}{\partial t} + \nabla \cdot (a_\mathrm{i} \boldsymbol{U}_\mathrm{i}) = \frac{2}{3}\left(\frac{a_\mathrm{i}}{\alpha}\right)\left(\frac{\partial \alpha}{\partial t} + \nabla \cdot \alpha \boldsymbol{U}_\mathrm{g} - \eta_\mathrm{ph}\right) \\ &+ \frac{1}{3\psi}\left(\frac{\alpha}{a_\mathrm{i}}\right)^2 \sum_j \boldsymbol{R}_j + \pi D_{bc}^2 R_\mathrm{ph} \end{aligned} \tag{11}$$

where a_i is the interfacial area concentration, representing the evolution of interfacial area per unit volume over time, $\boldsymbol{U}_\mathrm{i}$ denotes the interfacial velocity, α is the air phase fraction, $\boldsymbol{U}_\mathrm{g}$ is the air phase velocity, η_ph is the volume change source term due to phase change, which is not considered, ψ is a parameter related to the shape of the phase interface, which can be calculated as $1/36\pi$, D_bc denotes the characteristic bubble diameter, which is derived from the coalescence mechanism through the IATE source terms, $\boldsymbol{R}_j$ represents the source term for the mechanism of bubble interfacial area change induced by fluid flow. and R_j includes three forms: disintegration due to the impact of turbulent eddies, coalescence through random collision, and coalescence due to the acceleration of the following bubble in the wake of the preceding bubble.

2. Ship turbulence wake flow

2.1 *Ship model*

This study utilizes the JBC ship model released at the 2015 CFD Workshop on Ship Hydrodynamics held in Tokyo. A schematic of the geometry and coordinate system is presented in Fig. 1(a), while the principal dimensions of the model are summarized in Table 1. The geometric scale ratio of the model is 1:40.

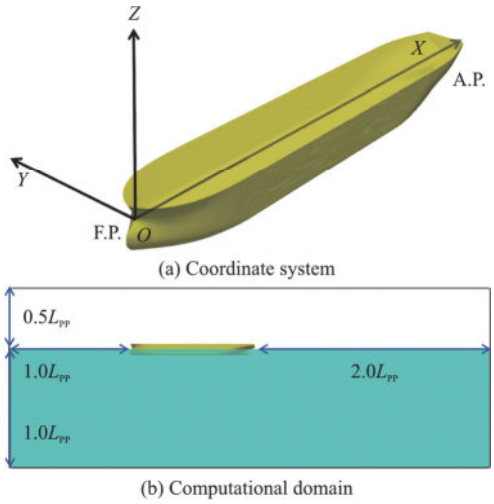

Fig. 1 Coordinate system and the computational domain (F.P. is the forward perpendicular, A.P. is the aft perpendicular)

Table 1 Principal dimensions of the JBC model

Principal dimensions	Model scale
Length between perpendiculars, L_pp / m	7.000
Length of waterline, L_WL / m	7.125
Maximum beam of waterline, B_WL / m	1.125
Displacement volume, ∇ / m^3	2.787
Draft, T / m	0.412 5
Depth, D_s / m	0.625 0
Wetted surface area, S_a / m^2	12.223
Block coefficient, C_B	0.858 0
Mid ship section coefficient, C_M	0.998 1
LCB ($\%L_\mathrm{pp}$), forward of midship	2.55
Vertical center of gravity (from keel), G_KB / m	0.3323

The standard model calculation in this study adopted a computational reference frame as shown in Fig. 1(b). The computational domain is defined as X/L_pp :[−1.0, 3.0], Y/L_pp :[−1.5, 1.5], Z/L_pp :[−1.0, 0.5], where X, Y, and Z are the streamwise, transverse, and vertical coordinates, respectively.

Three representative cross-sections in the stern wake region, S2 (X/L_{pp}=0.962 5), S4 (X/L_{pp}=0.984 3), and S7 (X/L_{pp}=1.000 0), are selected to investigate the down- stream evolution of the wake characteristics, as shown in Fig. 2.

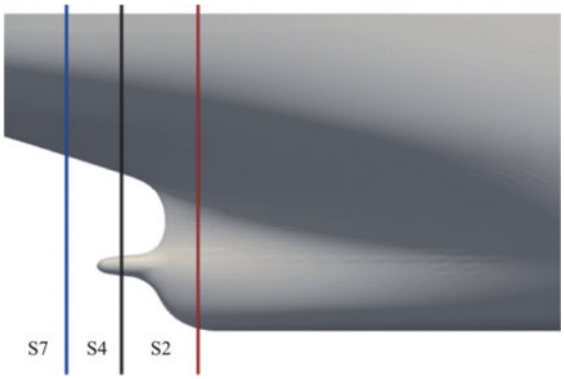

Fig. 2 Wake flow stations of JBC model (W2025 CFD workshop)

2.2 *Mesh*

The mesh generation was carried out using the *snappyHexMesh* tool within the open-source CFD platform OpenFOAM. A schematic of the computational domain and grid layout is shown in Fig. 3. The total number of cells is approximately 5.317×10^9. A structured grid was employed, and local grid refinement was applied near the free surface and in the stern region to account for the multiscale characteristics of the wake. The minimum grid spacing is Δx = 4.3 mm. The ship speed was set to V_m = 1.179 m/s corresponding to Froude number (Fr = 0.142) and Reynolds number ($Re = 7.46\times10^6$).

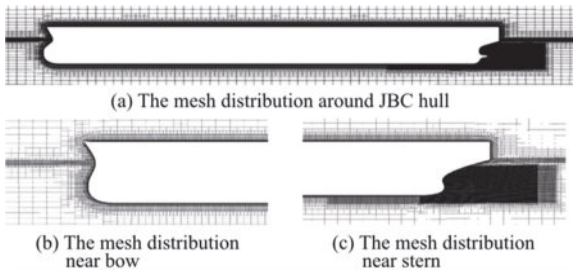

Fig. 3 The mesh distribution

For Sections S2, S4, and S7, enlarged views of the grid distribution and the filled contours of the ratio between the turbulence macro-scale ($L \approx k^{1.5}/\varepsilon$) and the local grid scale (Δ) are provided. Figure 4 present these enlarged views, where the contour distributions indicate the local L/Δ values. Regions with $L/\Delta > 1$ indicate that the turbulence macro-scale is larger than the local grid scale, suggesting that the dominant energy-containing motions associated with the coherent wake structures can be reasonably represented by the present simulation. The quantitative L/Δ ratios of the aft body vortices (ABV) at the selected sections are summarized in Table 2, further demonstrating that the turbulence macro-scales of the identified coherent structures are larger than the local grid scale. Although the dominant vortices are reasonably represented by the present spatial resolution, smaller-scale turbulent motions embedded within these coherent structures may still be affected by the grid resolution. Therefore, the present assessment mainly focuses on the capability of the grid to represent the dominant energy-containing range associated with the coherent wake structures.

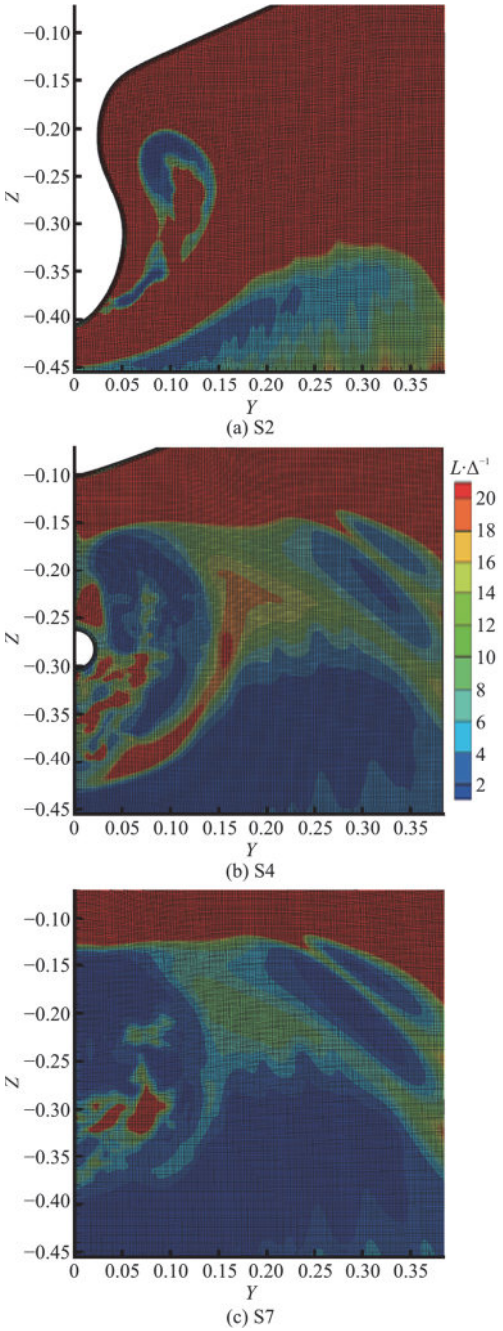

Fig. 4 Zoomed-in view of grid distribution overlaid with contours of the ratio of turbulence macro-scale (L) and grid-scale (Δ)

Table 2 L/Δ ratios of ABV at selected wake sections

Sections	ABV1	ABV2
S2	10.48	3.04
S4	14.73	4.87
S7	11.87	2.91

2.3 *Numerical results*

2.3.1 Resistance

The resistance coefficients of the JBC ship under the straight-ahead condition were calculated and compared with the experimental data from the JBC turbulence case of CFD Workshop 2025 held in Wageningen (Table 3). The predicted resistance coefficient shows good agreement with the experimental data, as reflected in the close matching of both the total resistance and its individual components. This consistency validates the reliability of the present numerical method and serves as a solid foundation for subsequent analyses and computational studies, such as wake turbulence characterization, vortex core tracking, and free-surface wave analysis.

Table 3 Comparison of ship resistance*

Parameters	C_T	C_F	$C_P \times 10^3$
EFD	4.290×10^3	3.160×10^3	1.13×10^3
CFD	4.330×10^3	3.100×10^3	1.23×10^3
$E\%D$	-0.932×10^3	1.899×10^3	-8.85×10^3

Note: C_T is the total resistance coefficient, C_F is the frictional resistance coefficient, C_P is the pressure resistance coefficient. *The validation can be done in the following way. The resistance is divided into pressure component and frictional component. For the measured data, $C_T \approx C_F + C_P$. Thus $C_{F,CFD}$ is compared with C_{F0} and $C_{P,CFD}$ with $C_T - C_{F0}$. The error analysis is done by using $E\%D = [(D-S)/D]\times100\%$, D is the experimental data, S is the corresponding CFD result.

FFT analysis is performed on the obtained resistance coefficients to extract their dominant frequencies. It can be seen from Fig. 5 that the dominant frequency of C_T is 0.545 Hz, that of lateral force coefficient (C_y) is 0.327 Hz, the dominant frequencies of vertical force coefficient (C_z) are 0.436 Hz and 1.417 Hz, and those of pitching moment coefficient (C_{My}) are 0.436 Hz and 1.417 Hz. The low frequency oscillation due to the wave celerity and model speed for captive towing tank testing can be estimated using the following equation, as shown in Doctors et al.[25]:

$$f = \frac{1}{T} = \frac{g}{8\pi U} = 0.330\ 7\ \text{Hz} \tag{12}$$

where f is the dominant frequency, T is the corresponding oscillation period, and U is the ship model.

This frequency is comparable to the dominant z and y force and My moment frequencies in the DDES results.

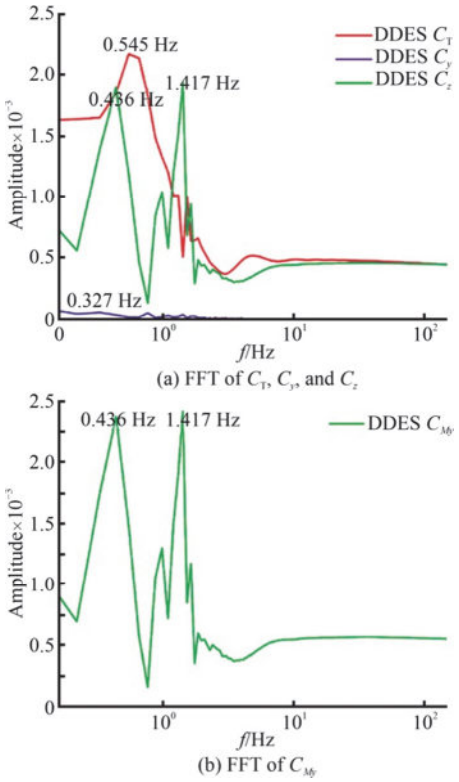

Fig. 5 FFT analysis of force coefficients

2.3.2 Wave pattern

As shown in Figs. 6-8, the overall free-surface prediction–including wave contours, wave profile, and longitudinal wave cuts–exhibits generally good agreement with the experimental data. The wave contours are well captured in terms of propagation direction and overall spatial extent, while the longitudinal wave cuts accurately reproduce the phase and amplitude of the dominant wave components.

However, the numerical simulation slightly overpredicts the wave elevation in the bow wave region. This discrepancy may result from the combined effects of free-surface deformation treatment, numerical dissipation, and the inherent limitations of interface-capturing methods in resolving localized wave-breaking features. Although further mesh refinement could potentially improve the prediction of local free-surface details, it would introduce substantially increased computational costs for the present scale-resolving simulation of the entire ship wake flow. Therefore, the current resolution represents a practical compromise between computational efficiency and the representation of the overall ship flow field.

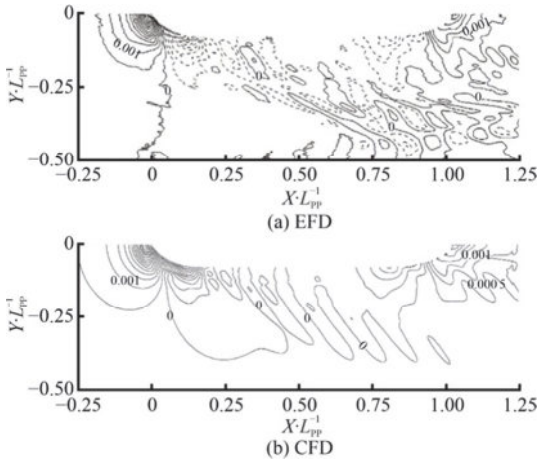

Fig. 6 Wave contours of the JBC stern wake

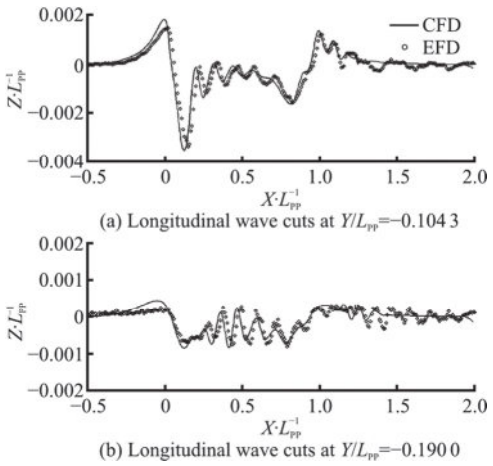

Fig. 7 Longitudinal wave cuts of the JBC stern wake

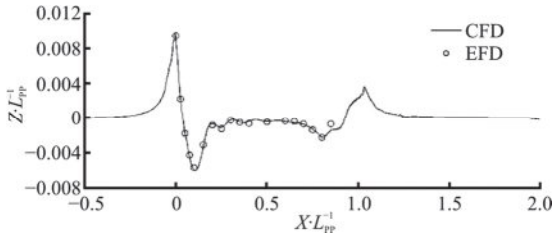

Fig. 8 Wave profile of the JBC stern wake

2.3.3 Velocity distribution

The wake velocity distributions of the JBC ship were investigated at three representative cross-sections (S2, S4, and S7) in the stern region. As shown in Fig. 9, the overall wake flow contour distributions agree well with the experimental results. However, the centerline recirculation region predicted by CFD appears slightly larger than that observed in the experiment. This discrepancy may be associated with the turbulent momentum transport and vortex-induced mixing characteristics predicted by the DDES approach. Since DDES resolves large-scale coherent structures while modeling smaller-scale turbulent motions, the representation of turbulent mixing and downstream wake recovery may be affected.

2.3.4 Flow separation

From the zoomed-in views in Fig. 10, converging streamlines and adverse pressure gradients are observed in the stern region. It can also be seen that the streamlines and wall shear stress are very complicated in the stern region. The adverse pressure gradient decelerates the near-wall flow, leading to regions where the wall shear stress approaches zero. These regions indicate flow separation, accompanied by reversed surface streamlines and the appearance of wall critical points. Within the separated region, nodes (N) and saddle points (S_p) are identified, and their respective numbers satisfy the classical topological rule for closed separation on an isolated 3-D body in a flow field, namely $N - S_p = 2$. This topological constraint characterizes the global pattern of surface streamlines in the separation zone and serves as an important criterion for assessing the physical consistency of numerical simulations.

2.3.5 Vortex analysis

In this study, the Q-criterion is adopted to identify the ABV vortical structures in the flow field. Figure 11 shows the isosurface at $Q = 10\ s^{-2}$, indicating the locations of the ABV1 and ABV2 vortices.

In this section, cross-section S4 is selected for vortex structure analysis. Located near the propeller plane in the stern region, this section lies within a highly complex flow zone where vortices are fully developed. On this plane, the morphology of the separated vortices, vortex core locations, and flow structures can be clearly identified. Since the inflow uniformity at the propeller plane directly affects propeller efficiency and excitation forces, a detailed analysis of the vortex structures at S4 is of significant engineering value, providing key information for propeller design and wake quality assessment.

The vortex core locations were identified using the Q-max method. For the ABV vortices in the S4 section, the vortex core velocities of ABV1 and ABV2 were extracted, as shown in Fig. 12. As shown in Fig. 13, the vortex core velocity of ABV1 is larger than that of ABV2, and the velocities of the two vortices exhibit periodic oscillations. The average vortex core axial velocity of ABV1 is 0.296 m/s, and that of ABV2 is 0.117 m/s.

Based on Taylor's frozen turbulence hypothesis, the energy spectra of ABV1 and ABV2 are obtained from the respective vortex core velocities[22]. As shown in Fig. 14, both spectra partially follow the −5/3 power law in the inertial subrange, indicating

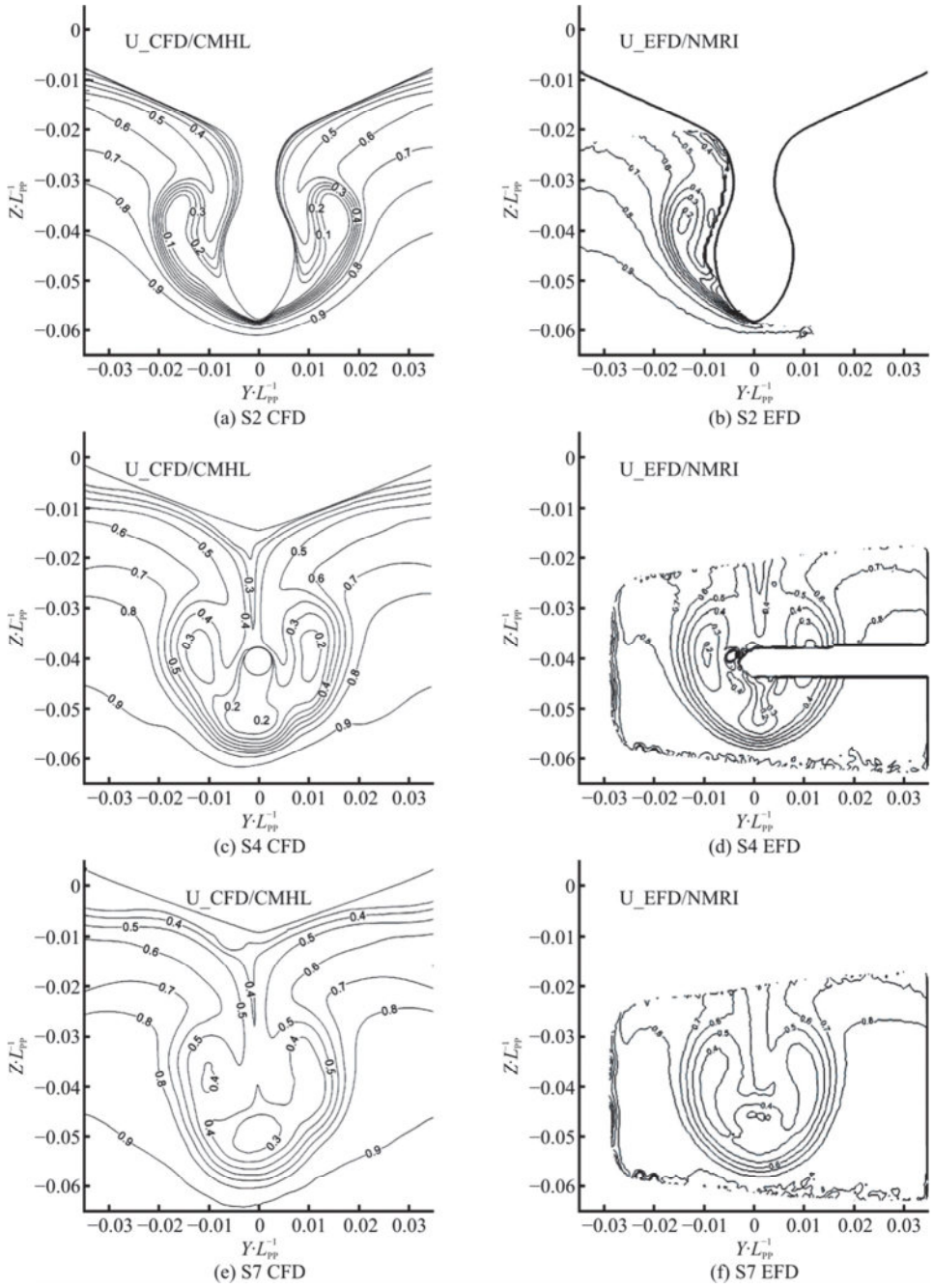

Fig. 9 Velocity distributions of the JBC stern wake

that the dominant energy transfer process is reasonably captured. The deviation observed at higher wavenumbers may result from the combined effects of limited spatial and temporal resolution, numerical dissipation, and the possible deviation of Taylor's frozen turbulence hypothesis under highly unsteady wake conditions. This defines the resolved spectral range of the present simulation. Within that range, the simulation reliably captures the energy-containing scales and the coherent vortex structures (ABV1 and ABV2) in the JBC wake.

3. Ship air-mixed wake flow

3.1 *Ship model and computational setup*

The ship model investigated in this study is a specially designed VLCC equipped with an air layer drag reduction system on its bottom. The model has a length between perpendiculars (L_{pp}) of 7 m and a design speed of 15 knots. At model scale, the experimental speed is 1.117 m/s.

The air layer device on the ship's bottom consists of two main components. The first is a longitudinal air

barrier, and the second is wedge-shaped structures at the bow and stern. The bow wedge is designed to induce flow separation, facilitating air accumulation and layer formation after injection from the holes. The stern wedge serves to promote air layer accumulation and stabilize the mixed flow exiting the bottom air layer region, as shown in Fig. 15.

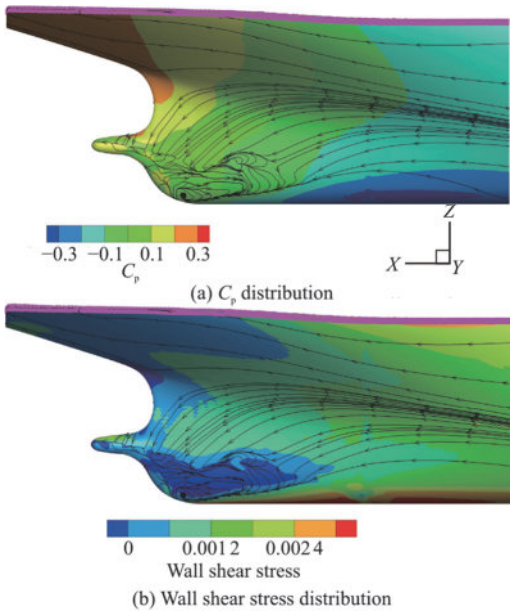

Fig. 10 Pressure distributions of stern region with surface lines

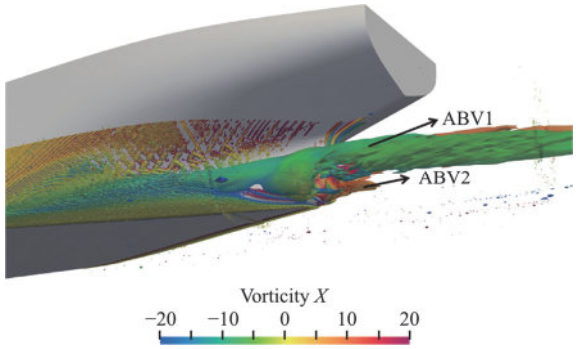

Fig. 11 ABV vortical structures in the stern region of JBC

Three rows of air injection holes are arranged on the ship's bottom. The number of holes in each row is 8, 10, and 10. The injection velocities for the numerical simulations are derived by equating the flow area and volumetric flow rate, resulting in: 1.915 m/s, 0.5347 m/s, and 0.8377 m/s. A double-model approach is adopted, in which the computational domain covers only the submerged part of the hull with its top boundary located at the undisturbed waterline.

The gravity direction is aligned with the z-axis, and the flow direction corresponds to the x-axis. The top boundary of the domain is aligned with the waterline and treated as a symmetry plane. The domain extends $4L_{pp}$ in the streamwise direction, $1L_{pp}$ in depth, and $1L_{pp}$ in width. The bow is located at $x=0$, positioned $1L_{pp}$ downstream from the domain inlet, as shown in Fig. 16.

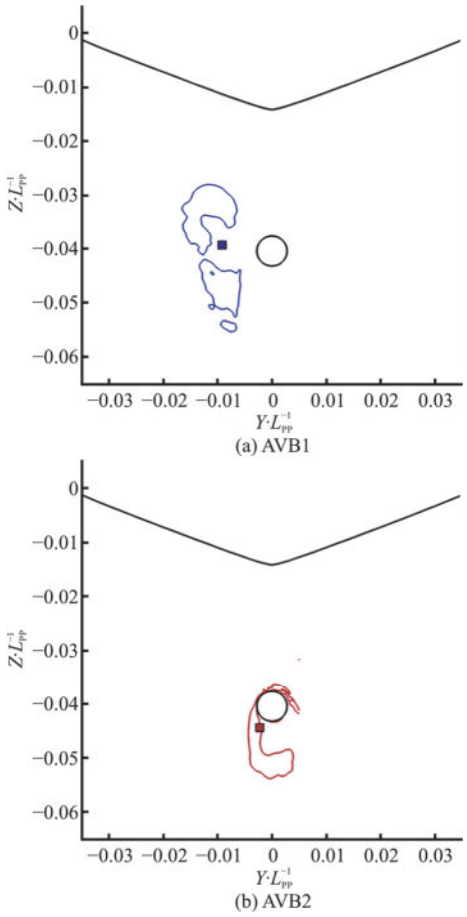

Fig. 12 ABV vortex core locations at S4

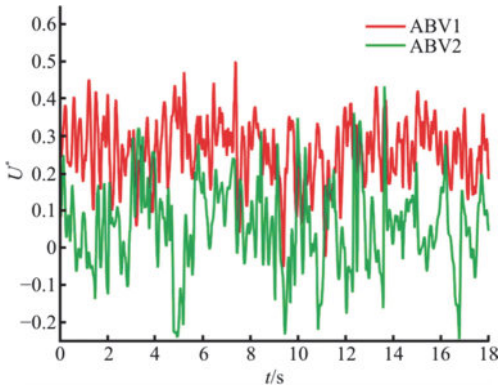

Fig. 13 ABV vortex core normalized axial velocity (U^*) at S4

The computational mesh is generated using the snappyHexMesh utility in OpenFOAM. The total number of cells is approximately 1.25×10^9, and average dimensionless wall distance (y^+) is approximately 60. Since the study primarily focuses on the stern flow field, additional mesh refinement is applied in the stern region, as shown in Fig. 17.

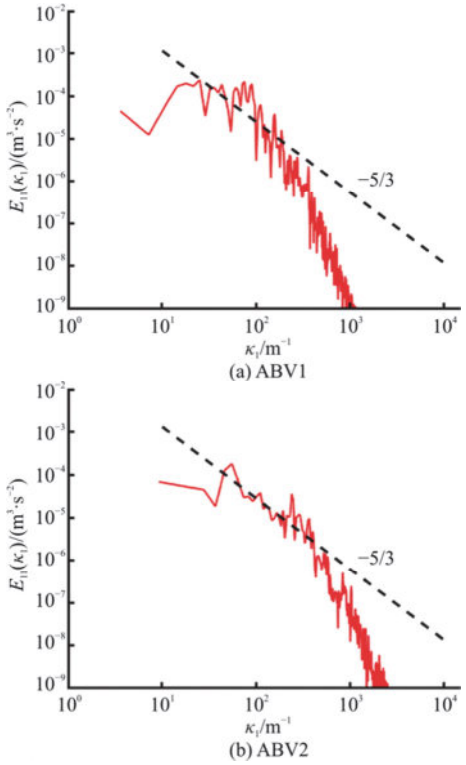

Fig. 14 Energy spectra of ABV vortex at S4

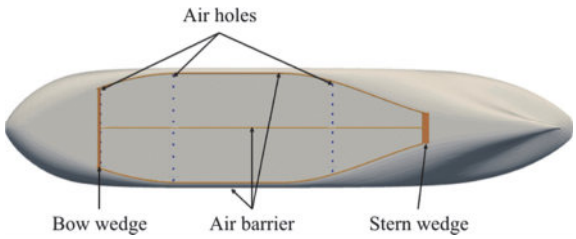

Fig. 15 Bottom air layer device and air holes

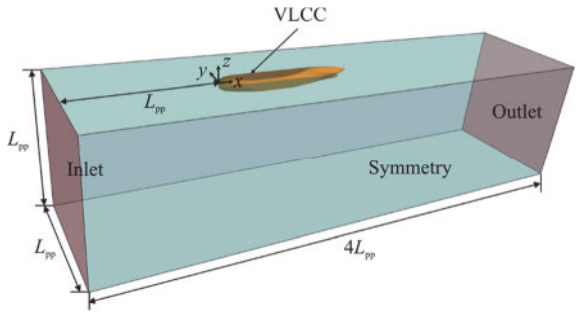

Fig. 16 Computational domain setup

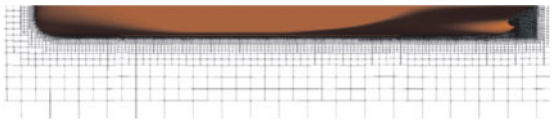

Fig. 17 Computational mesh around VLCC hull

3.2 *Numerical results*

3.2.1 Velocity distribution

The stern velocity distribution of a VLCC ship with air layer drag reduction is investigated. Referring to the analysis of the three sections of JBC, the three corresponding stern sections are determined as S1, S2, and S3, with positions as follows, S1: $X/L_{pp} = 0.941\,4$, S2: $X/L_{pp} = 0.955\,0$, and S3: $X/L_{pp} = 0.964\,3$, and comparisons are made with the case without air injection.

As can be seen from the velocity contour of the mean flow at the stern in Fig. 18, the changes in the stern flow field induced by air-layer drag reduction are remarkably significant. In the absence of air injection, the mean velocity distribution at the stern resembles that of the JBC, with a low-velocity region near the ship hull surface due to frictional effects, accompanied by typical vortex shedding characteristic of separated flow. At the hub of Section S2, an asymmetric velocity distribution is observed between the upper and lower parts, with lower velocities occurring below the hub. After air injection, the original velocity distribution undergoes noticeable changes: the extent of the low-velocity region is significantly reduced and becomes more confined to the immediate vicinity of the hull surface. The vortex shedding phenomenon observed at Section S1 disappears, replaced by a relatively smooth velocity envelope, where the flow velocity increases rapidly from the wall in the normal direction. Similarly, the same trends are observed at Sections S2 and S3. These results indicate that the aerated wake generated by air-layer drag reduction has a pronounced influence on the stern flow field, and the associated reduction in frictional drag leads to a diminished low-velocity region near the stern hull surface and around the hub.

As can be seen from the mean velocity contours and streamlines in Fig. 19, when the wake contains air, the streamlines at the stern exhibit a certain upward shift in the z-direction. This is because the air-liquid mixture generated by air injection, upon flowing to the stern, rises away from the hull surface from the bottom and sides of the ship. The upward motion of the air induces a certain upward velocity in the surrounding water, thereby manifesting as an overall upward trend in the stern velocity. Unlike the upward deviation of streamlines in single-phase flow caused by the stern geometry contraction, the degree of streamline deviation under aerated conditions is more pronounced.

3.2.2 Air fraction distribution

To investigate the flow characteristics of the aerated wake at the ship stern, Fig. 20 presents the instantaneous contour of the air phase fraction distribution at the stern. The isosurface corresponds to an air phase fraction of 0.5, colored by the air phase

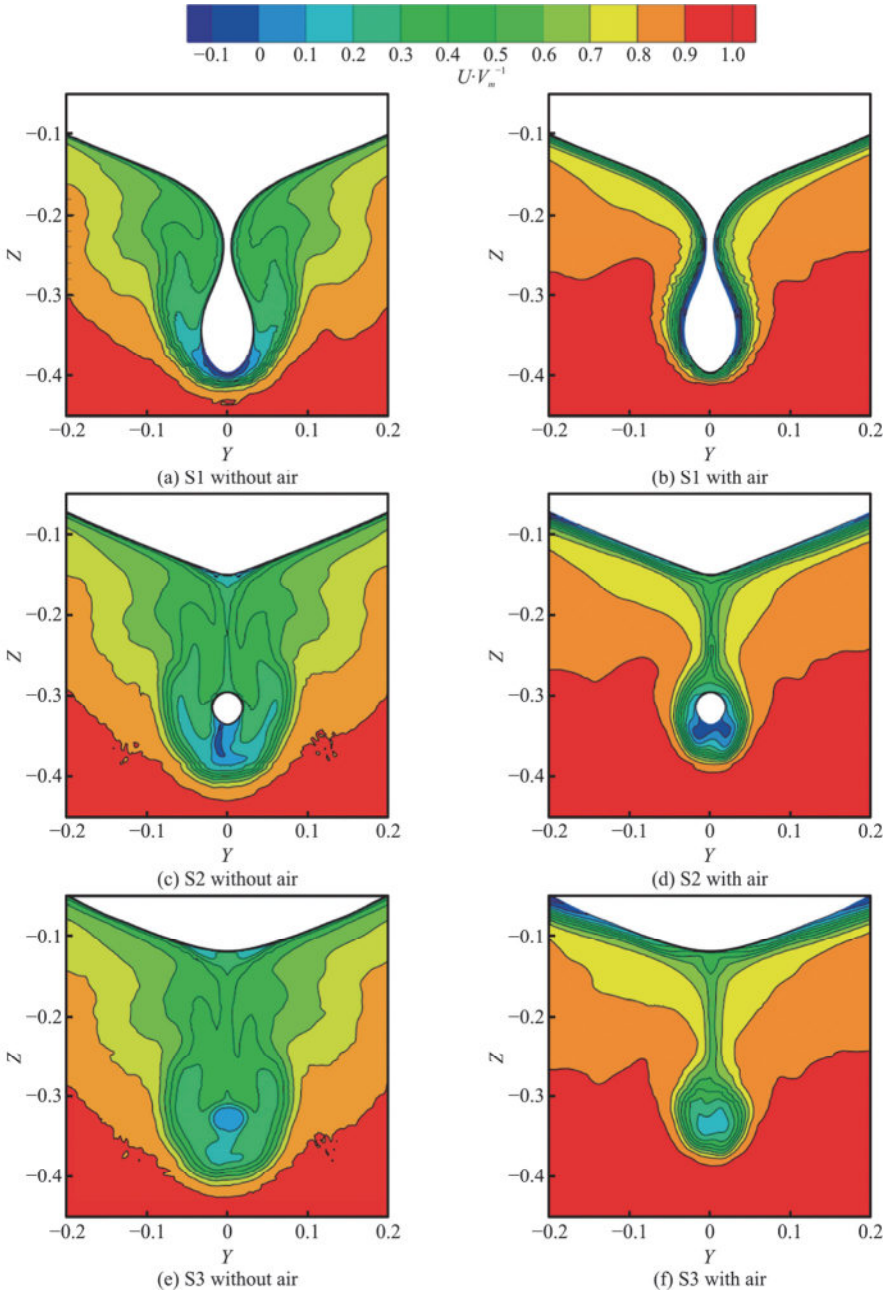

Fig. 18 Velocity distributions of the VLCC stern wake (U / V_{m} represents the dimensionless velocity ratio, V_{m} is the characteristic velocity)

velocity.

As can be seen from Fig. 20(b), most of the air generated by air-layer drag reduction rapidly rises along the wall on both sides of the stern. From the air velocity distribution, it is evident that the air velocity becomes significantly higher on both sides of the stern due to the superposition of the ascending velocity and the water flow velocity, and most of the air rapidly ascends and diffuses in these regions. Nevertheless, a small amount of air remains in the form of discrete bubbles and is carried downstream by the water flow, eventually entering the propeller flow field.

As can be seen from Fig. 21, although most of the air rapidly rises along the wall on both sides of the stern, a portion of the air is still carried downstream by the water flow and eventually enters the propeller flow field. At Section S1, a certain amount of air remains attached to the near-wall region, with a relatively high local air fraction. At Section S2 (which is already within the propeller disk plane), a certain amount of air is still present. The air fraction near the hub, which is 0.453%, remains relatively high. As the distance from the hull increases, the air fraction gradually decreases. The air fraction at S1 is 1.246%

and at S3 is 0.224%.

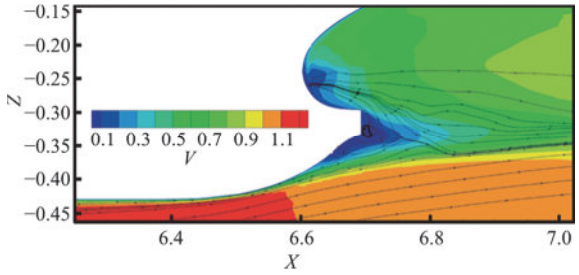

Fig. 19 Contours of mean velocity and streamlines at the stern under aerated condition (xz- plane)

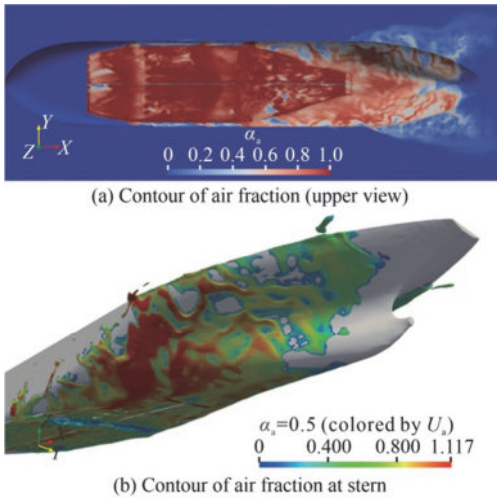

Fig. 20 Instantaneous contour of air fraction around the ship

3.2.3 Wake fraction

Figure 22 shows the contour of the mean wake fraction at the propeller disk plane (S2). It is evident that after applying air layer drag reduction, the mean wake fraction decreases significantly, and the high wake fraction region becomes closer to the hull surface. This indicates that the air layer drag reduction reduces the frictional resistance of the ship, thereby decreasing the drag effect by the hull on the surrounding fluid.

Table 4 shows the calculated results of the mean wake fraction at the propeller disk plane. It can be seen that, compared with the experimental data, the calculation error under the non-aeration condition is relatively small, only 6.89%, with the numerical simulation results being slightly higher. Under the aeration condition, the calculation error is 9.6%, with the numerical simulation results being slightly lower. The increase in error is attributable to two main factors. On one hand, the use of separate turbulence models for the air and water phases leads to a superposition of errors. On the other hand, the air phase is modeled as equivalent spherical particles without accounting for complex physical processes such as bubble deformation, which further exacerbates the error.

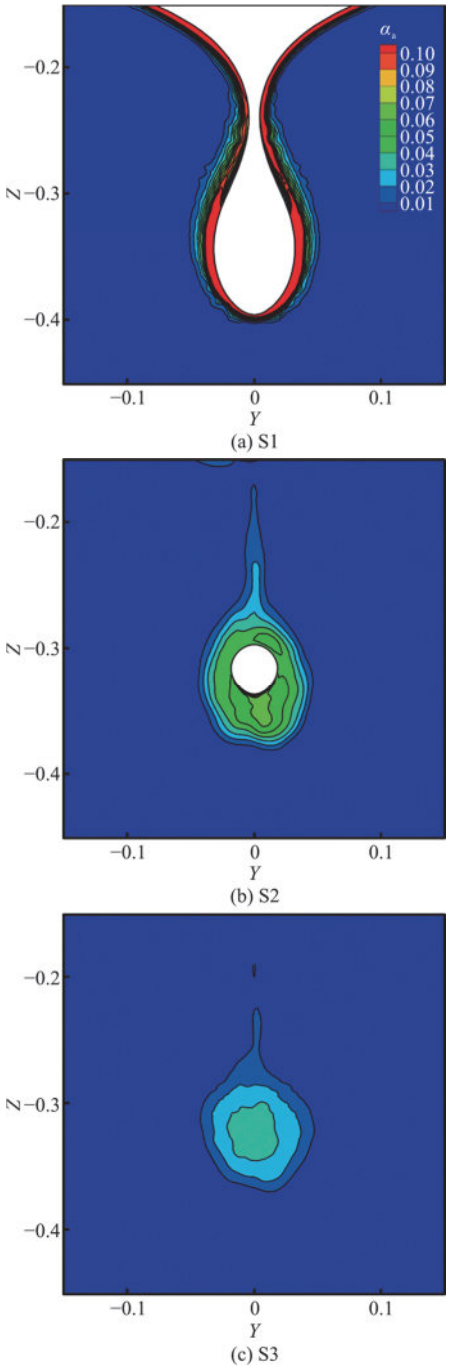

Fig. 21 Contours of the mean air phase fraction (α_a) at stern sections S1, S2, and S3

The average wake fraction after using air layer drag reduction decreases by approximately 40% in the experiment and 50% in the numerical simulation. Considering the total number of grids used in the calculation and the simplifications made compared to the experiments, it can be considered that the numerical simulation method employed in this study achieves relatively high computational accuracy. It can also be observed from the results that the mean

wake fraction decreases significantly after the application of air layer drag reduction, indicating that the air-liquid mixed wake has a significant effect on the flow field around the propeller. However, the specific impact of the reduced wake fraction on propeller propulsion performance requires further targeted investigation, taking into account the combined effects of inflow air fraction and variations in inflow velocity.

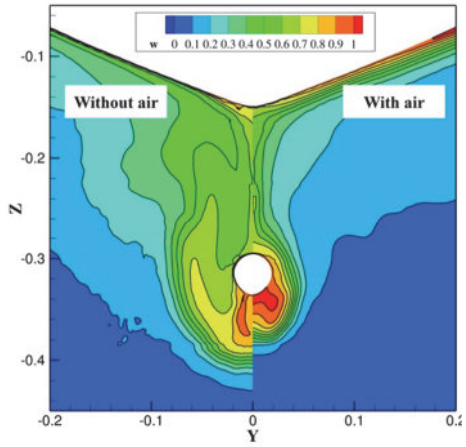

Fig. 22 Contour of the mean wake fraction (w) at the propeller disk plane under the non-aeration and aeration conditions

Table 4 Comparison of the mean wake fraction at the propeller disk plane (S2)

Mean wake fraction	Exp.	CFD	Error/%
Without air	0.296	0.316	6.89
With air	0.175	0.158	9.6

4. Conclusions

In this study, the DDES method based on the SST k-ω turbulence model is employed to simulate the flow field around the JBC model. The predicted resistance coefficients under straight-ahead condition agree well with experimental data, demonstrating the capability of the present numerical approach. Wave-pattern predictions are generally consistent with experiments, except that the bow wave amplitude is slightly overpredicted. The stern wake velocity distributions at sections S2, S4 and S7 show general agreement, but the centerline recirculation zone is overpredicted. Zoomed-in views reveal converging streamlines, adverse pressure gradients, and regions of vanishing wall shear stress, confirming flow separation. The observed nodes and saddle points satisfy the topological rule $N - S_p = 2$, confirming the physical consistency of the simulated separation pattern. The Q-criterion identifies ABV1 and ABV2 vortices. At the propeller plane (section S4), the vortex core velocity of ABV1 (mean 0.296 m/s) is larger than that of ABV2 (0.117 m/s), and both exhibit periodic oscillations. Based on Taylor's frozen turbulence hypothesis, the energy spectra of the two vortices partially follow the –5/3 power law in the inertial subrange. The deviation at higher wavenumbers may be associated with the combined effects of spatial and temporal resolution limitations, numerical dissipation, and the possible deviation of Taylor's frozen turbulence hypothesis under highly unsteady wake conditions, which define the resolved spectral range of the present simulation. Within that range, the simulation reliably captures the energy-containing scales and the coherent vortex structures (ABV1 and ABV2) in the JBC wake.

The Euler-Euler two-fluid method was employed to investigate the air-mixed wake of a ship with air-layer drag reduction. The feasibility of this numerical approach for solving air-liquid mixing problems was validated. Most of the air generated by air-layer drag reduction rapidly rises along the wall on both sides of the stern. Under the combined action of buoyancy and water flow drag, the air velocity on both sides of the stern is relatively high. Some of the air is entrained downstream by the water flow in the form of discrete bubbles, enters the propeller flow field, and exerts a certain influence on the velocity distribution at the propeller disk plane. Because of the effect of air-layer drag reduction, the flow beneath the hull is characterized by large-scale air-liquid mixing. Under this flow condition, the frictional resistance on the hull wall is reduced, ultimately leading to changes in the velocity distribution at the stern. Compared with single-phase flow, the mean flow velocity at the stern under aerated conditions is higher, and the region of low velocity is smaller, indicating that air-layer drag reduction has a significant impact on ship resistance.

Nevertheless, the present study is limited in terms of the available spatiotemporal resolution for ship turbulence wake flow and in the validation of scale effects on air-mixed wake flow. Future research will focus on improving the spatiotemporal resolution and conducting more thorough studies of scale effects on air-mixed flows, thereby advancing the understanding and prediction of ship turbulence wake flows.

Conflict of interest

All authors declare that there are no other competing interests.

References

[1] Shevchuk I, Sahab A, Abdel-Maksoud M. Experimental and numerical studies of the flow around the JBC hull form at straight ahead condition and 8 degrees drift angle [C]//*33rd Symposium on Naval Hydrodynamics*, Osaka, Japan (virtual), 2020.

[2] Stern F, Sanada Y, Starman Z, et al. 4DPTV measurements and DES of the turbulence structure and vortex breakdown and interaction for 5415 sonar dome vortices [C]//*35th Symposium on Naval Hydrodynamics*, Nantes, France, 2024.

[3] Jiang Z, Hirdaris S, Tavakoli S, et al. A CFD study on the hydrodynamic response of a small-scale ice floe induced by a passing ship [J]. *Journal of Hydrodynamics*, 2024, 36(2): 290-299.

[4] Ge G, Zhang W, Xie B, et al. Turbulence model optimization of ship wake field based on data assimilation [J]. *Ocean Engineering*, 2024, 295: 116929.

[5] Grlj C G, Degiuli N, Martić I. Scale effects on the resistance and propulsion characteristics of the Japan Bulk Carrier [J]. *Ocean Engineering*, 2025, 339: 122059.

[6] Queutey P, Guilmineau E, Visonneau M, et al. RANS and hybrid RANS-LES simulations around the Japan Bulk Carrier of the Tokyo 2015 CFD Workshop [C]//*19th Numerical Towing Tank Symposium*, St. Pierre d'Oléron, France, 2016.

[7] Xing T, Bhushan S, Stern F. Vortical and turbulent structures for KVLCC2 at drift angle 0, 12, and 30 degrees [J]. *Ocean Engineering*, 2012, 55: 23-43.

[8] Fureby C, Toxopeus S L, Johansson M, et al. A computational study of the flow around the KVLCC2 model hull at straight ahead conditions and at drift [J]. *Ocean Engineering*, 2016, 118: 1-16.

[9] Feder D F, Shevchuk I, Sahab A, et al. Characteristics and consequences of vortex wandering around a ship hull at drift: A numerical study [J]. *Ocean Engineering*, 2022, 255: 111220.

[10] Johansen J P, Castro A M, Carrica P M. Full-scale two-phase flow measurements on Athena research vessel [J]. *International Journal of Multiphase Flow*, 2010, 36(9): 720-737.

[11] Mizokami S, Kawakita C, Kodan Y, et al. Experimental study of air lubrication method and verification of effects on actual hull by means of sea trial [J]. *Mitsubishi Heavy Industries Technical Review*, 2010, 47(3): 41-47.

[12] Wang H, Wang K, Liu G. Drag reduction by gas lubrication with bubbles [J]. *Ocean Engineering*, 2022, 258: 111833.

[13] Zhang X, He K, Wan D. Research progress on mechanism and numerical simulation methods of water-air-bubble mixed flow around marine structure [J]. *Chinese Journal of Ship Research*, 2022, 17(3): 1-28(in Chinese).

[14] Kannan Y S, Karri B, Sahu K C. Letter: Entrapment and interaction of an air bubble with an oscillating cavitation bubble [J]. *Physics of Fluids*, 2018, 30(4): 041701.

[15] Deane G B, Stokes M D. Scale dependence of bubble creation mechanisms in breaking waves [J]. *Nature*, 2002, 418(6900): 839-844.

[16] Kimmoun O, Branger H. A particle image velocimetry investigation on laboratory surf-zone breaking waves over a sloping beach [J]. *Journal of Fluid Mechanics*, 2007, 588: 353-397.

[17] Carrica P M, Drew D, Bonetto F, et al. A polydisperse model for bubbly two-phase flow around a surface ship [J]. *International Journal of Multiphase Flow*, 1999, 25(2): 257-305.

[18] Castro A M, Li J, Carrica P M. A mechanistic model of bubble entrainment in turbulent free surface flows [J]. *International Journal of Multiphase Flow*, 2016, 86: 35-55.

[19] Li J, Martin J E, Carrica P M. Large-scale simulation of ship bubbly wake during a maneuver in stratified flow [J]. *Ocean Engineering*, 2019, 173: 643-658.

[20] Zhao X, Hao Y, Cui J, et al. Numerical investigations on drag reduction by micro-bubbles of KVLCC2 ship model by means of OpenFOAM [J]. *Ocean Engineering*, 2025, 122609.

[21] Kawaita K, Takano S, Kodan Y, et al. Experimental investigation of the behavior of injected air on the ship bottom and its influence on propeller [J]. *Journal of the Kansai Society of Naval Architects, Japan*, 2010(12): 43-50.

[22] Wang Z, Gu J, Qian H. The impact of actively injecting bubbles on propeller performance [J]. *Ocean Engineering*, 2025, 333: 121518.

[23] Wang C, Wu G, Wang D, et al. Numerical study of flow features around submerged circular and square piles at flat and scoured beds using OpenFOAM [J]. *Journal of Ocean University of China*, 2024, 23(4): 897-914.

[24] Bhushan S, Yoon H, Stern F. Detached eddy simulations and tomographic PIV measurements of flows over surface combatant 5415 at straight-ahead and static drift conditions [J]. *Ocean Engineering*, 2021, 238: 109658.

[25] Doctors L J, Day A H, Clelland D. Unsteady effects during resistance tests on a ship model in a towing tank [J]. *Journal of Ship Research*, 2008, 52(4): 263-273.